A new global marine gravity model NSOAS24 derived from multi-satellite sea surface slopes

Shengjun Zhang[1*], Xu Chen[1], Runsheng Zhou[1], Yongjun Jia[2*]

[1] School of Resources and Civil Engineering, Northeastern University, Shenyang, China

[2] National Satellite Ocean Application Service, Beijing, China

Correspondence to: Shengjun Zhang (zhangshengjun@whu.edu.cn) and Yongjun Jia (jiayongjun@mail.nsoas.org.cn)

Abstract

Judging from the early release of the NSOAS22 model, there were some known issues, such as boundary connection problems in block-wise solutions and a relatively high noise level. By solving these problems, a new global marine gravity model NSOAS24 is derived based on sea surface slopes (SSS) from multi-satellite altimetry missions. Firstly, SSS and along-track deflections of vertical (DOV) are obtained by retracking, resampling, screening, differentiating, and filtering procedures on basis of altimeter waveforms and sea surface height measurements. Secondly, DOVs with a 1'x1' grid interval are further determined by the Green's function method, which applies directional gradients to constrain the surface, least-square fit to constrain noisy points, and tension constraints to smooth the field. Finally, the marine gravity anomaly is recovered from the gridded DOV according to the Laplace Equation. Among the entire processing procedures, accuracy improvements are expected for NSOAS24 model due to the following changes, e.g., supplementing recent mission observations and removing ancient mission data, optimizing the step size during the Green's function method, and special handling in near-shore areas. These optimizations effectively resolved the known issues of signal aliasing and the "hollow phenomenon" in coastal zones. The typical altimetry-derived marine gravity models are the DTU series released by the Technical University of Denmark and the S&S series released by the Scripps Institution of Oceanography (SIO), University of California San Diego (UCSD). Their latest models, DTU21 and SS V32.1, were used for comparison and validation. Numerical verification was conducted in three experimental areas (Mariana Trench area, Mid-Atlantic Ridge area, Antarctic area, representing low, mid and high latitude zones) with DTU21, SS V32.1 and shipborne data. Taking NSOAS22 for

contrast, NSOAS24 showed improvements of 1.2, 0.7, 1.0 mGal in 3 test areas by validating with SS V32.1, while declines of 0.6, 0.5, 0.3 mGal, and 0.2, 0.4, 0.3 mGal occurred in STD statistics with DTU21 and shipborne data. Finally, the NSOAS24 was assessed using two sets of shipborne data (the early NCEI dataset and the lately dataset from JAMSTEC, MGDS, FOCD, and SHOM) on global scale. Generally, NSOAS24(6.33 and 4.95 mGal) showed comparable accuracy level with DTU21 (6.20 and 4.71 mGal) and SS V32.1 (6.40 and 5.53 mGal), and better accuracy than NSOAS22 (6.64 mGal and 5.64 mGal). Besides, the new model is available at https://doi.org/10.5281/zenodo.12730119 (Zhang et al., 2024).

1 Introduction

Satellite altimetry provides highly accurate ocean surface height measurements with respect to certain ellipsoids along corresponding ground tracks (Fu and Cazenave, 2001; Stammer and Cazenave, 2017). Among these altimetry satellites, some have performed geodetic missions (GM) with longer revisit period and denser spatial coverage, which provide the primary data sources for marine gravity recovery. Exact repeat missions (ERM) are also critical in relevant researches according to a relatively lower noise level by averaging nonunique, repetitive cycles (Zhang et al., 2022). Due to new altimetry technology and advanced processing methods, the accuracy of sea surface height (SSH) has increased dramatically over the last decade (Andersen et al., 2023), with a positive influence on marine gravity model construction. The refinement of altimetry-derived marine gravity model has become more obvious due to these recent altimetry missions with dense spatial coverage since 2010, e.g., CryoSat-2, SARAL/AltiKa, Jason-1, Jason-2 and HY-2A GM (Chen et al., 2024). Combining observations from multiple satellites with different orbital inclinations such as 108°, 98°, 92°, and 66° enables a more reliable determination of the marine gravity field (Andersen et al., 2019; Sandwell et al., 2021). In addition to conventional nadir altimeters, synchronized laser beams for obtaining reflected surface height information, two-satellite companion mode, and wide-swath altimetry techniques offer new observations and require effective incorporating strategies for modeling marine gravity field. Furthermore, these advancements provide new opportunities and potentials for recovering refined marine gravity anomalies. Generally, combining multi-frequency and multi-mode altimetry data, especially these observations with higher range accuracy, denser spatial coverage, and diverse track directions, is an effective way of refining marine gravity recovery (Sandwell et al., 2021).

China launched Haiyang-2A (HY-2A) satellite in 2011 and initiated its geodetic mission in 2016 for the purpose of geodetic applications. Multiple previous studies have shown that the HY-2A has consistent accuracy with other conventional altimetry missions (Wan et al., 2020; Zhang et al., 2020; Guo et al., 2022b). Moreover, its followers including HY-2B, HY-2C, and HY-2D were successively launched in 2018, 2020, 2021. Although the HY-2 data cannot serve as the sole input for constructing a 1′x1′ marine gravity anomaly model (Wan et al., 2020; Zhang et al., 2022), the HY-2 series of measurements are extremely valuable for recovering marine gravity anomalies

because of their unique spatial distributions. Currently, several institutions have effectively adopted HY-2 series data to release regional or global marine gravity models, such as the SCSGA V1. 0 (Zhu et al., 2020), the NSOAS22 (Zhang et al., 2022), the GMGA1 (Wan et al., 2022), the SDUST2021GRA (Zhu et al., 2022), and the GMGA2 (Hao et al., 2023). Leaving aside the HY-2 series, the most well-known altimetry-derived marine gravity models are DTU and S&S series, which are respectively released by the Technical University of Denmark and the Scripps Institution of Oceanography (SIO), University of California San Diego (UCSD). To some extent, they represent the highest attainable accuracy (Li et al., 2021; Mohamed et al., 2022). Their latest versions have been updated to DTU21 and S&S V32.1.

In a previous study of releasing NSOAS22 model, we primarily evaluated the performance of HY-2 series altimeter data in constructing marine gravity fields and highlighted the role played by HY-2. However, we found some obvious issues identified in the NSOAS22 through systematic evaluation. The first and foremost is the boundary connection problem in block-wise solutions, which lead to a sawtooth-like discontinuity in the final recovered marine gravity signals. Therefore, this paper aims to address existing issues and to optimize the model-construction steps for the purpose of constructing refined marine gravity model. These specific improvements contain dataset filtering and optimization (supplementing recent observations and removing low-quality data), re-designing the step sizes for solving DOV with Green's functions, and special processing in near-shore areas. These improvements will be further described in detail in Section 4.

Besides, the remainder of this paper is organized as follows. Section 2 provides a general description of the involved datasets (altimeter data and shipborne data), as well as the reference gravity models used for comparison and remove-restore procedure. The theoretical methods for DOV calculation and gravity anomaly inversion are presented in Section 3. Section 5 evaluates the altimetry-derived global marine gravity model using the well-known altimetry derived models and shipborne measurements. Finally, conclusions are given in Section 6, focusing on the 1'x1' global marine gravity anomaly model named NSOAS24.

2 Research data

2.1 Altimetry data

The newly accumulated altimetry data has not only provided high-quality SSH observations

but also diverse spatial distributions. For these recent missions, we selected the sensor geophysical data records (SGDR), which include high-sampling waveforms from the Jason-1, Jason-2, Jason-3, Cryosat-2, HY-2A, HY-2B, and SARAL/AltiKa. In addition, Jason-1, Jason-2, and SARAL/AltiKa adopt both ERM and GM data, HY-2A only uses GM data, while HY-2B and Jason-3 only use ERM data. Cryosat-2 data comprise three modes: low-resolution mode (LRM), synthetic aperture radar (SAR), and synthetic aperture radar interference (SIN). Taking in account the previously collected dataset, Geosat observations from both GM and ERM with unique 108° orbital inclination angle, along with ERS-1 GM, Envisat and TOPEX/Poseidon ERM datasets, were also utilized. Envisat acquired ERM data for two repeated periods, 30 days and 35 days. The detail information of involved altimetry data is listed in Table 1.

Table 1. Information of altimetry satellites used for deriving gravity field.

Mission	Satellite	Period	Inclination (°)
Geodetic mission	Jason-1	2012.05-2013.06	66.00
	Jason-2	2017.09-2019.10	66.00
	CryoSat-2	2010.07-2019.04	92.00
	SARAL/AltiKa	2016.07-2024.01	98.55
	HY-2A	2016.03-2019.06	99.30
	Topex/Poseidon	2002.07-2006.10	66.00
	Geosat	1985.04-1986.11	108.10
	ERS-1	1994.04-1995.05	98.52
Exact repeat mission	Jason-1	2008.08-2012.03	66.00
	Jason-2	2008.07-2017.05	66.00
	Jason-3	2016.02-2020.07	66.00
	SARAL/AltiKa	2013.03-2016.07	98.55
	HY-2B	2018.11-2023.11	99.30
	EnviSat	2002.05-2012.04	98.55
	Topex/Poseidon	1992.10-2002.06	66.00
	Geosat	1986.12-1990.01	108.10

Along-track SSS can be considered as vector data, and its magnitude is determined by the time interval between adjacent ground track points and corresponding SSH variations. Due to different design of satellite orbital inclinations and ground track orientations (ascending or descending), along-track SSS capture different signal variations and similar signal variation magnitude with opposite signs. As shown in Figure 1, satellites with different orbital inclinations exhibit significant

112 differences in along-track slopes obtained in the Mariana Trench area. Ascending and descending

113 orbit data both reflect the overall regional trend, exhibiting horizontal symmetry in direction and

114 being numerically nearly opposite. For instance, the orbital inclination of HY-2A is approximately

115 99°, allowing it to obtain actual data reaching up to around 81° in high-latitude regions. In contrast,

116 other altimetry satellites are limited by their designed orbital parameters, such as the Jason series,

117 which cannot measure data beyond the 66° region. Satellites with near polar orbit have a data

118 coverage advantage in high-latitude regions. Considering the spatial coverage and orientations, the

119 calculated slopes should be stored separately based on different orbital inclinations and directions

120 to ensure the consistency. Consequently, we categorized these satellites in Table 1 into 5 groups

121 based on their orbital design, as shown in Table 2. For multi-cycle data, these are appended to the

122 same data file without disrupting temporal continuity, preparing for subsequent segment-based slope

123 editing steps.
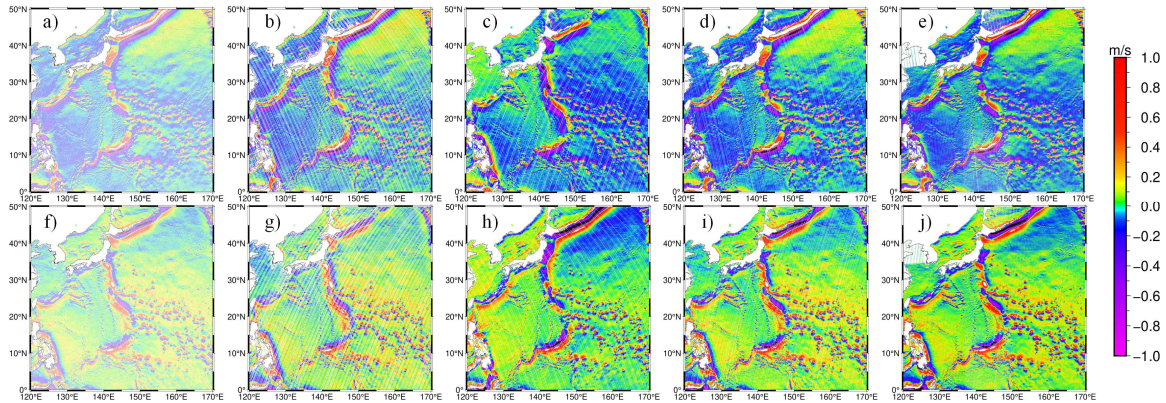
124

125 **Figure 1.** Slope plot of satellite ascent/descent at different orbital inclinations (a, b, c, d, e

126 represent ascending track slopes for HY-2A (99.3°), Geosat (108°), Jason-2 (66°), SARAL/AltiKa

127 (98.55°), CryoSat-2 (92°) respectively; f, g, h, i, j represent descending track slopes for HY-2A,

128 Geosat, Jason-2, SARAL/AltiKa, CryoSat-2 respectively).

129 **Table 2.** Grouping of satellites according to different orbital inclinations.

i(108°)	ii(98.55°)	iii(66°)	iv(92°)	v(99.3°)
Geosat (GM)	Envisat	TOPEX	CryoSat-2(SAR)	HY-2A(GM)
Geosat (ERM)	Envisat-P	TOPEX-M	CryoSat-2-P(SAR)	HY-2B(ERM)
	SARAL/AltiKa(GM)	Jason-1(GM)	CryoSat-2(SIN)	
	SARAL/AltiKa(ERM)	Jason-1(ERM)	CryoSat-2-P(SIN)	
	SARAL/AltiKa-F	Jason-2(GM)	CryoSat-2(LRM)	
		Jason-2(ERM)		
		Jason-3(ERM)		

2.2 Typical gravity models

To compare and validate the new global marine gravity model, several well-known models are introduced. Firstly, the latest version of the S&S series model V32.1, which includes both DOV and gravity anomaly, is used for comparison and validation purposes, hereinafter referred to as the V32.1. Secondly, the DTU21 gravity anomaly model is introduced for comparison and validation. Thirdly, the classical EGM2008 comprehensive series model is introduced, which provides the SSH along with DOT2008A mean dynamic topography model, DOV, and gravity anomaly (Pavlis et al., 2012). It serves as the reference model in the remove-restore procedure.

2.3 Shipborne data

Firstly, a total of 10,740,231 ancient shipborne data points were collected from NCEI (National Centers for Environmental Information). Secondly, a total of 33,522,351 recent measurements from four marine institutions with relatively high quality were gathered: FOCD (French Oceanographic Cruises Directory), JAMSTEC (Japan Agency for Marine-Earth Science and Technology), MGDS (Marine Geoscience Data System), and SHOM (French Naval Hydrographic and Oceanographic Service). The distribution of shipborne data is illustrated in Figure 2. The NCEI data covers global oceans more comprehensively, whereas non-NCEI data exhibits dense coverage in the nearby regions of Japan and in the partial Antarctic seas. Due to inevitable outliers in in-situ data, necessary data editing was conducted using the triple standard deviation criterion by calculating deviations with respect to the EGM2008 model. As shown in Figure 2(c), three regions, which are marked in dashed rectangles and span low, mid, and high-latitude oceans (Area1: 0°-50°N, 120°-170°E; Area2: 10°-60°N, 310°-360°W; Area3: 50°-80°S, 180°-300°W), were selected as experimental areas.
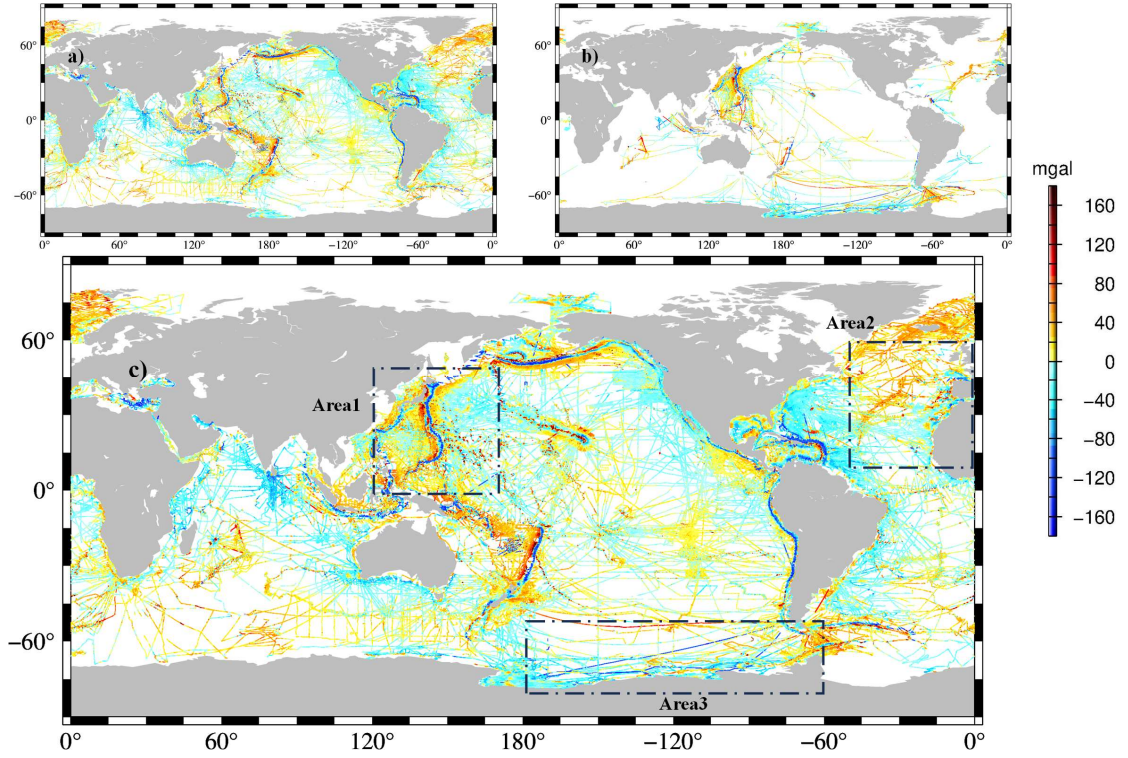
Figure 2. Distribution of shipborne data (a: NCEI; b: FOCD, JAMSTEC, MGDS, SHOM;

c: Total shipborne data, with three experimental areas highlighted in dashed rectangles).

3. Theoretical methodology

3.1 Method of along-track DOV calculation

Instead of the derivative of the geoid with respect to the spherical distance, Sandwell et al. (1997) proposed a method of calculating along-track DOV with two steps. Firstly, geoid slopes were derived from adjacent geoid heights and corresponding temporal variations. Secondly, the along-track DOV is computed on basis of geoid slopes by dividing by corresponding satellite orbit parameter derived velocity. The procedure is summarized in following formula.

$$\varepsilon^{\alpha} = -\frac{\partial N}{\partial s} = -\frac{\partial N}{\partial t} * \frac{\partial t}{\partial s} = -\frac{\partial N}{\partial t} * \frac{1}{v} \tag{1}$$

Here, N is the height of the geoid, s is the spherical distance, and t is the observation time. The process for determining the linear velocity v is as follows. Given a data point's latitude φ, we first convert the geodetic latitude to geocentric latitude φ_c by considering the Earth's flattening e. The formula is expressed as follows:

$$\varphi_c = \frac{1-e}{\sqrt{cos^2\varphi + (1-e)^4 sin^2\varphi}} \tag{2}$$

Assuming the inclination angle of the satellite's orbit is α, the period of the orbit's descending

168   node is T, the regression period is t, the distance between adjacent trajectories is s, and the

169   equatorial circumference is L, the average angular velocity w_s and synchronous Earth velocity w_e

170   of the satellite's elliptical motion along the orbit can be calculated separately

171
$$w_s = \frac{2\pi}{T} \tag{3}$$

172
$$w_e = \frac{w_s t L}{s} \tag{4}$$

173   Subsequently, the angular velocity components w_φ and w_λ along the latitude and longitude

174   directions can be obtained separately

175
$$w_\varphi = \frac{w_s \cos^2 \varphi}{(1-e)^2 \cos^2 \varphi_c} \sqrt{1 - \frac{\cos^2 \alpha}{\cos^2 \varphi_c}} \tag{5}$$

176
$$w_\lambda = \frac{w_s \cos \varphi}{\cos^2 \varphi_c} - w_e \tag{6}$$

177   Simple synthesis can obtain the angular velocity w along the orbit

178
$$w = \sqrt{w_\varphi{}^2 + w_\lambda{}^2} \tag{7}$$

179   Finally, multiply by the radius of the Earth R to obtain the ground linear velocity v

180
$$v = wR \tag{8}$$

181 **3.2 Method of gridded DOV calculation**

182   The Green's method proposed by Wessel et al. (1998) restores the along-track DOV to the

183   gradient direction of the geoid, and subsequently projects it onto the prime (east-west) and

184   meridional (north-south) components, achieving a similar transformation in the along-track

185   components (Brammer et al., 1980).

186   For a linear operator L, the output or response under the action of a point source δ is the Green's

187   function G,

188
$$LG = \delta \tag{9}$$

189 where L is taken as the Laplace operator ∇^2,

190
$$\nabla = i\frac{\partial}{\partial x} + j\frac{\partial}{\partial y} + k\frac{\partial}{\partial z} \tag{10}$$

191   The Green's function formulation transforms to

192
$$\nabla^2 \phi(x) = \delta(x) \tag{11}$$

193   The left-hand side of the above equation represents the product of the Laplace operator and

194   the Green's function formulation, while the right-hand side corresponds to the Dirac delta function.

195   Solutions that satisfy the Laplace equation are known as harmonic functions, corresponding to cases

196   where the divergence is zero. The formulation for biharmonic functions is introduced as follows:

197    $$\nabla^4 \phi(x) = \delta(x) \tag{12}$$

198   Splines interpolation, whether in one or two dimensions, corresponds physically to enforcing

199   a thin elastic beam or plate to conform to data constraints. The same interpolation principles apply

200   to the two-dimensional Green's function formulation as follows:

201    $$D\nabla^4 \phi(x) - T\nabla^2 \phi(x) = \delta(x) \tag{13}$$

202   In the equation, D represents stiffness, and T denotes tension factor.

203   In the discrete case, the following equation holds when there are M reference points within

204   the region:

205    $$D\nabla^4 w(x) - T\nabla^2 w(x) = \sum_{j=1}^{M} c_j\, \delta(x - x_j) \tag{14}$$

206   Wessel et al. (1998) derived the solution $w(x)$ through Fourier transformation as:

207    $$w(x) = \sum_{j=1}^{M} c_j\, \phi(x - x_j) \tag{15}$$

208    $$\phi(x) = K_0(p|x|) + \log(p|x|) \tag{16}$$

209   When there are N known points within the region, the following equation matrix can be

210   constructed:

211    $$w_i = \sum_{j=1}^{M} c_j\, \phi(x_i - x_j) \quad i = 1, N \tag{17}$$

212   Thus,

213    $$w = Gc \tag{18}$$

214   The along-track DOV is the projection of the gradient of the geoid along the track direction.

215   The inverse solution is obtained using the Green's function method, simultaneously applying tension

216   spline functions to ensure curve smoothness. The fundamental concept is to simulate the geoid field

217   using a finite number of control points. This approach aims to interpolate and recover the DOV at

218   all grid points. In discrete conditions, the Green's method formula is shown as equation (14), where

219   the left-hand side represents selected control points and the right-hand side consists of other known

220   points with radial basis functions. By iteratively solving from the known points towards the control

221   points, the radial basis coefficients c_j are determined. This process can be viewed as constructing

222   the geoid field ϕ using finite elements.

223   Considering that $\phi(x)$ and w_i are scalar fields representing the geoid and their corresponding

224   geoid heights, and the actual input data represents the directional derivatives of the geoid,

225   specifically the along-track DOV vector information. Therefore, introducing the gradient field

226        $grad\phi(x)$ is formulated as follows in equation (19):

$$\nabla\phi(x) = \mathrm{i}\frac{\partial\phi}{\partial x} + \mathrm{j}\frac{\partial\phi}{\partial y} + \mathrm{k}\frac{\partial\phi}{\partial z} \tag{19}$$

$$s_i = (\nabla w \cdot n)_i = \sum_{j=1}^{M} c_j\, \nabla\phi(x_i - x_j) \cdot n_i \quad i = 1, N \tag{20}$$

$$\boldsymbol{D} = \sum_{j=1}^{M} c_j\, \nabla\phi(x_i - x_j) \quad i = 1, N \tag{21}$$

230   When simultaneously taking the directional derivative in the satellite operation direction n_i on

231   both sides, s_i represents the along-track DOV vector. $\nabla\phi(x)$ corresponds to the gradient field of the

232   geoid. Considering the varying quality of data from different satellites, uncertainties sig are

233   incrementally added to control data quality. Therefore, an equation matrix can be constructed at

234   reference points:

$$\begin{bmatrix} s_1/sig_1 \\ \vdots \\ s_n/sig_n \end{bmatrix} = \begin{bmatrix} c_1 \\ \vdots \\ c_m \end{bmatrix}^T \begin{pmatrix} 0 & \cdots & D_{x_1-x_m} n_1/sig_1 \\ \vdots & \ddots & \vdots \\ D_{x_n-x_1} n_n/sig_n & \cdots & 0 \end{pmatrix}^T \quad i = 1, N \; j = 1, M \tag{22}$$

236   After solving for the coefficients c_j, the construction of the geoid gradient field is completed.

237   At any grid point, the geoid gradient $\boldsymbol{D}$ can be determined. Multiplying this gradient by the east-

238   west and north-south directional vectors yields the DOV components at each grid point.

239   The Green's function method offers several advantages. Firstly, it innovatively applies

240   directional gradients rather than SSH to constrain the model surface, in order to enhance stability.

241   Secondly, it employs least squares fitting instead of exact interpolation, effectively mitigating the

242   impact of noisy data points. Additionally, by incorporating tension constraints, it facilitates data

243   smoothing. For moderate data volumes, the Green's function method is superior to traditional finite

244   difference methods. However, Green's functions also present certain limitations, such as their

245   inability to handle excessively large datasets, challenges with boundary discontinuities, and

246   suboptimal performance in near-shore areas. These issues will be discussed and addressed in Section

247   4.

248   **3.3 Method of deriving gravity anomalies**

249   The relationship between DOV and gravity disturbances or anomalies can be deduced by the

250   Laplace equation (Sandwell and Smith 1997). The relationships are established according to the

251   internal connections among the disturbing potential T , gravity disturbances δg , gravity anomaly

252   Δg , and two directional components of DOV (ξ and η). Assuming a flat Earth approximation, the

253   disturbing potential T satisfies the Laplace equation in the given local planar coordinate system (x,

254   y, z). Then, the relationship between gravity and DOV can be established as the following equation.

255
$$\frac{\partial \delta g}{\partial z} = -\Upsilon_0 \left(\frac{\partial \xi}{\partial x} + \frac{\partial \eta}{\partial y} \right) \tag{23}$$

256   Taking the difference between gravity disturbance and gravity anomaly into account, the gravity

257   anomaly is further calculated according to,

258
$$\Delta g(x,y) = \delta g(x,y) - \frac{2\Upsilon_0}{R} N(x,y) \tag{24}$$

259   where R is the average radius of Earth, and N is the geoid height, which can be provided by geo-

260   potential models. For the detailed computation procedure, please refer to Zhang et al. (2020).

261   **4 Model construction**

262   Based on the theories summarized in Section 3, we sequentially calculated along-track SSH,

263   SSS, along-track DOV, gridded DOV and gridded gravity anomalies from multi-frequency and

264   multi-mode satellite altimetry data. For the purpose of model construction, a series of joint

265   processing strategies, e.g., waveform retracking, adding corrections, resampling, data editing,

266   filtering, as well as the remove-and-restore procedure were necessary. The specific construction

267   steps are illustrated in Figure 3.
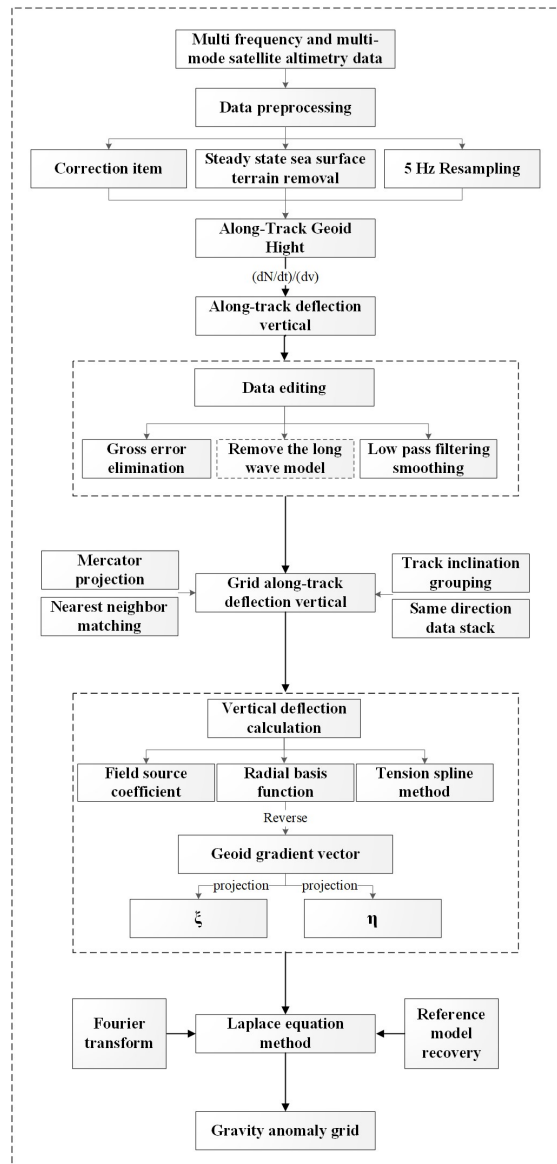
269 **Figure 3**. Flowchart of constructing marine gravity model from multi-satellite altimeter data.

4.1 Data preprocessing and slope editing

Firstly, raw waveforms were retracked using the two-step weighted least-square retracker (Zhang and Sandwell, 2017), and high-rate observations along profiles were uniformly resampled into 5 Hz to constrain the noise level and enhance the density of available measurements. Secondly, along-track SSH measurements were calculated by adding correction items provided in the SDR products to amend corresponding effects for path delay and geophysical environment. Then the along-track slopes were calculated, and their accuracy was validated with the EGM2008 model slopes. If the deviations exceed the setting threshold according to the triple standard deviation criterion, the data point is considered unreliable and removed. If excessive data segments are edited

279   out, the entire segment is abandoned to prevent the influence of outliers on subsequent calculations.

280   Finally, a Parks–McClellan filter was applied to all slopes to constrain the amplified high-frequency

281   noise during the difference procedure. Marine gravity models derived from conventional nadir

282   altimeters achieve an accuracy of approximately 2–3 mGal and require low-pass filtering at

283   wavelengths of at least 14 km to suppress short-wavelength noise (Sandwell et al., 2021). Based on

284   this standard, we used a Parks–McClellan filter with a cutoff wavelength of 16 km.

285   **4.2 Gridding along-track DOV**

286   Firstly, along-track velocities corresponding to different satellites were calculated to convert

287   along-track slopes to along-track DOV. Then along-track residual DOVs were computed by filtering

288   the EGM2008 geoid heights and corresponding DOT2008A_n180 mean dynamic topography.

289   Before gridding, it is necessary to define the objective grid in advance. Considering that the

290   inversion grid should closely resemble the real earth, a Mercator projection grid was chosen in this

291   study. The Mercator projection is a cylindrical map projection that preserves angles and is used for

292   a 1'×1' global grid, with 21,600 grid points in both latitude and longitude directions (The latitude

293   direction uses the Gudermannian function transformation, while the longitude direction is uniformly

294   divided). After defining the gridding points, along-track slopes were gridded using a nearest-

295   neighbor approach. Satellites are categorized based on orbital inclination and ground track

296   orientation, which ensures that the along-track DOV direction remains consistent and averages

297   potentially redundant data points in the same direction at grid points, thereby reducing data

298   complexity. Due to the requirements of the Green's function method regarding region size and data

299   volume, the convergence of multiple vectors with different values at the same gridding points but

300   with consistent directions can lead to matrix singularity. It is worth mentioning that the averaging

301   step between each category was essential to address this issue.

302   As mentioned above, along-track DOVs were mapped to gridding points. Taking the HY-2

303   group for instance, the gridding process for ascending and descending track segments is illustrated

304   in Figure 4. Matching is performed using the nearest-neighbor method, and data stacking follows

305   the principle of consolidating data in the same direction. The specific process is summarized as

306   follows. (1) Determine the number and position of 1'×1' grid points implemented using the Mercator

307   projection. (2) Project the geodetic latitude and longitude of input data to Mercator coordinates, and

308   determine the nearest grid point in the Mercator coordinate system for each data point. (3) Perform

309   weighted averaging for data in the same direction, and store data from different groups separately.
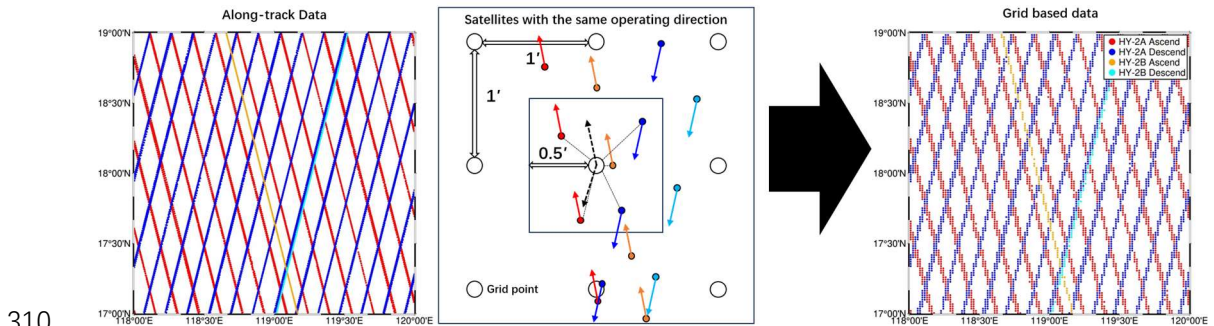
311   **Figure 4.** Gridding along-track DOVs at grid points (HY-2 group for example).

312   **4.3 DOV components calculation**

313   Limited by the computing power of computer and massive gridding points, the DOV

314   components were calculated with block-wise input and output to avoid excessive computational

315   redundancy and matrix singularity. While constructing NSOAS22 model, the tension spline method

316   overlooked the impact of coherence between block-wise regions. This tension spline interpolation

317   is typically suitable for solving small to moderate-sized regions with medium data volumes.

318   However, excessive data can drastically reduce computational efficiency and potentially cause stack

319   overflow issues. Consequently, constraints arising from the distribution of known points may lead

320   to ineffective solving at boundaries and discontinuities between adjacent regions, as illustrated in

321   Figure 5(a). In this study, we proposed a new solution by enlarging computation regions while

322   restricting output to central areas to ensure continuity. Specifically, the inputs were chosen within a

323   64*64 grid, and the outputs were exclusively limited to the central 32*32 grid. As illustrated in

324   Figure 5(b), the discontinuous effect was eliminated.
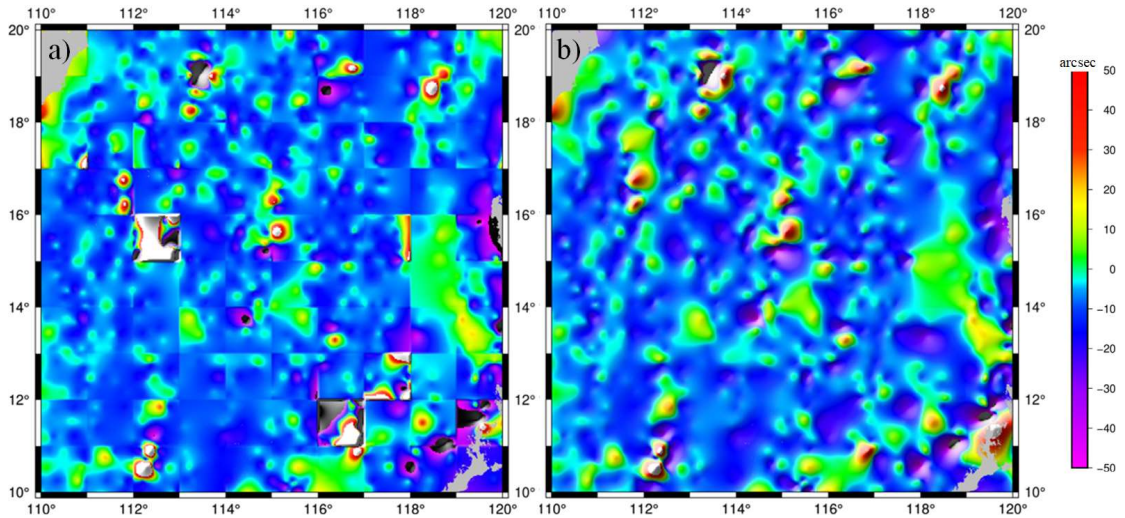
Figure 5. Result of spline splicing method for DOV east-west components (a: original; b: new).

4.3.1 Step selection

To compute DOV components using the Green's function method, it is necessary to select specific grids as control points for iterative processes. The graphical representation of solving DOV components using the Green's function method is illustrated in Figure 6. Additionally, the tension spline interpolation demonstrates optimal performance when control points are evenly distributed. Leveraging the regularity of the grid, the step size (interval between two control points) is defined for selecting control points. An increased number of control points tends to render the spline curve more rigid, thereby accentuating large fluctuations and noise. Conversely, a reduced number of control points leads to a sparser spline curve that appears smoother, effectively mitigating noise. However, sparse control points may result in an overly simplistic representation of the field. As control points become sparser, the interpolation distance increases, thereby reducing the reliability of the results.
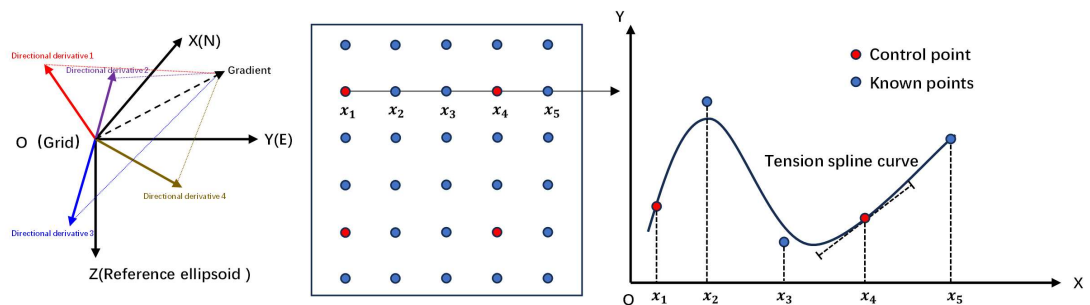
Figure 6. Green's function method for solving DOV components.

Our computational grid size is 64*64, offering different control point densities based on step

342   sizes: 4096 control points with step size 1, 1024 with step size 2, and 441 with step size 3. Larger

343   step sizes lead to fewer control points, which may not adequately represent the region. Step size 1

344   results in excessive noise, affecting signal continuity and computational efficiency. Hence, step sizes

345   2 and 3 are under consideration in our study for balancing detail and computational feasibility.

346   In experimental area 1 in Figure 2(c), the residual DOV for step sizes 2 and 3 is shown in

347   Figure 7. The figure demonstrates that with a step size of 2, noticeable noise artifacts are introduced,

348   particularly impacting the east-west components. In contrast, using a step size of 3 results in

349   smoother outcomes, exhibiting clearer distribution characteristics of the DOV components. The

350   reduction of noise is particularly effective in specific areas like near-shore regions and islands.

351
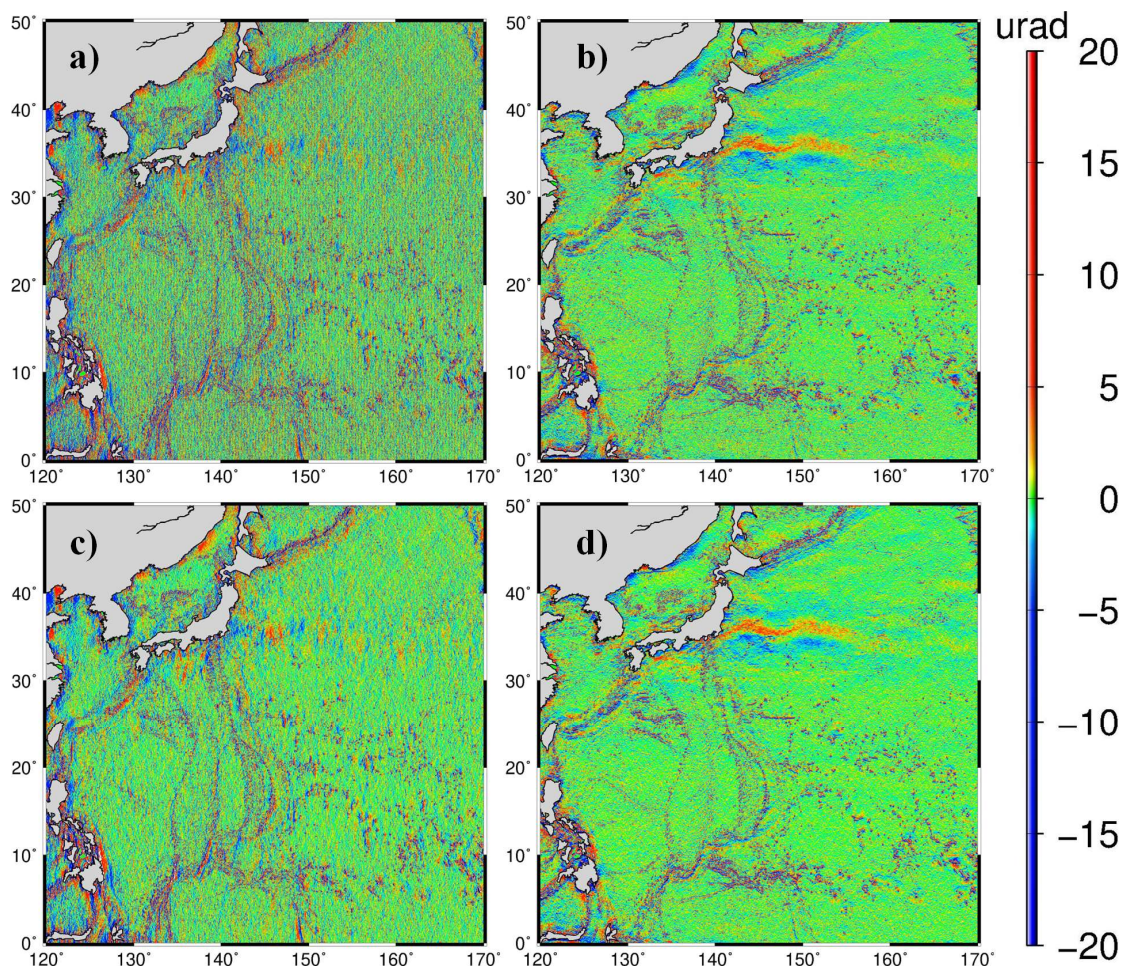
Figure 7. Residual results of DOV components difference for different step size selections (a: east-west component at 2 steps; b: north-south component at 2 steps; c: east-west component at 3 steps; d: north-south component at 3 steps).

355   Then we analyzed the distribution of noise under different step sizes. The V32.1 serves as a

356   verification model, against which the DOV results obtained with a step size of 2 are subtracted. The

357   standard deviation is 3.19 µrad for the east-west component and 2.02 µrad for the north-south

358 component. Setting a threshold based on the triple standard deviation criterion, the primary noise

359 locations are depicted in Figure 8(a) and (b). There are 125,456 noise points in the east-west

360 component, accounting for 1.20% of the entire region, and 122,976 noise points in the north-south

361 component, making up 1.19% of the total area. After removing these noise points, the standard

362 deviations reduce to 2.45 μrad for the east-west component and 1.36 μrad for the north-south

363 component. With a step size of 3, the standard deviations are respectively 2.37 μrad for the east-

364 west component and 1.75 μrad for the north-south component. Identifying based on the triple

365 standard deviation criterion, the primary noise locations are shown in Figure 8(c) and (d). There are

366 77,904 noise points in the east-west component, accounting for 0.75% of the entire region, and

367 105,923 noise points in the north-south component, comprising 1.02% of the total area. After

368 removing outliers, the standard deviations decrease to 1.84 μrad for the east-west component and

369 1.20 μrad for the north-south component.

370 The noise histogram with different step sizes, as shown in Figure 9, provides a more intuitive

371 demonstration that a step size of 3 effectively reduces noise compared to a step size of 2. Notably,

372 the east-west component exhibits a noticeably reduction in noise when using a step size of 3.

373 Moreover, scattered noise points in open ocean areas are massively eliminated. This is to say, the

374 selection of step size significantly influences both the distribution and magnitude of noise points.

375 Considering on larger step size's advantages in enhanced computational efficiency, reduced matrix

376 complexity, and lower mitigate noise, we finally selected step size 3 for acquiring controlling points.
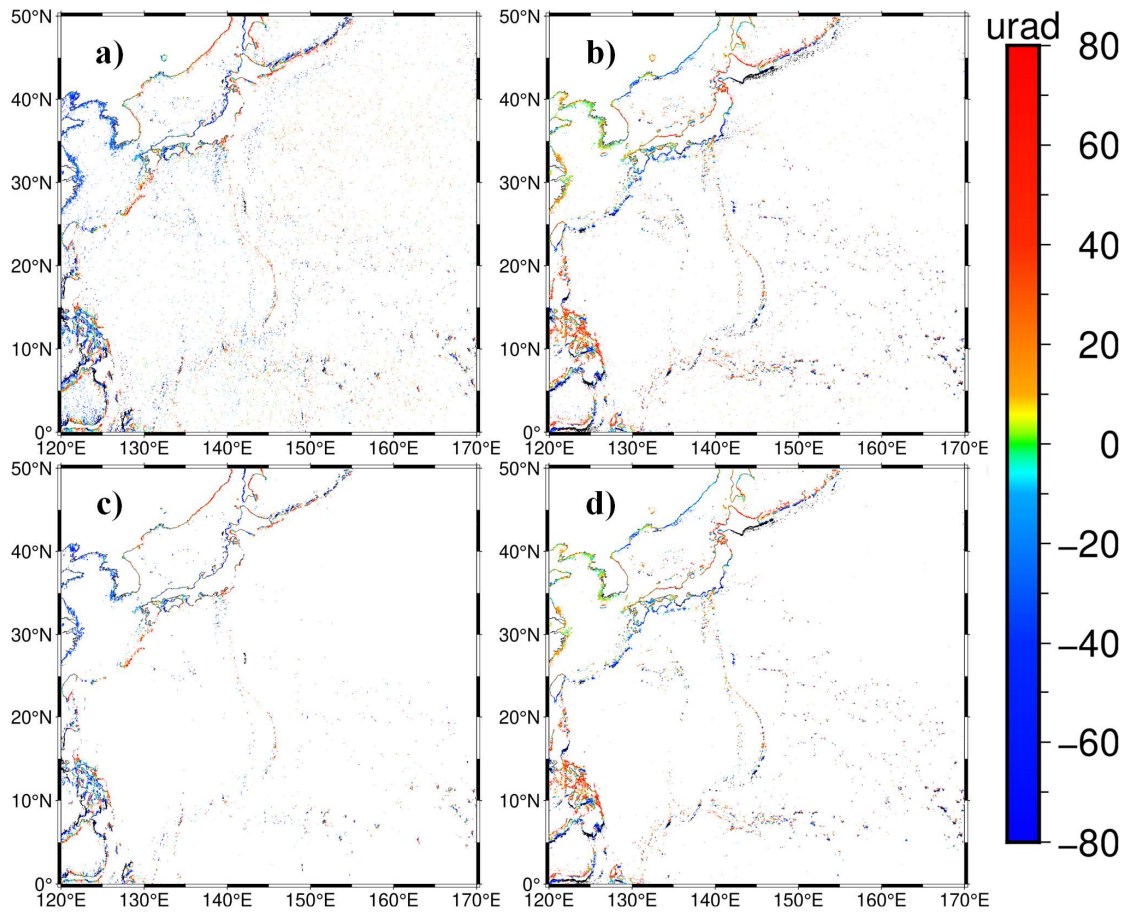
Figure 8. Noise analysis at different step sizes (a: east-west component at step size 2; b: north-south component at step size 2; c: east-west component at step size 3; d: north-south component at step size 3).

381
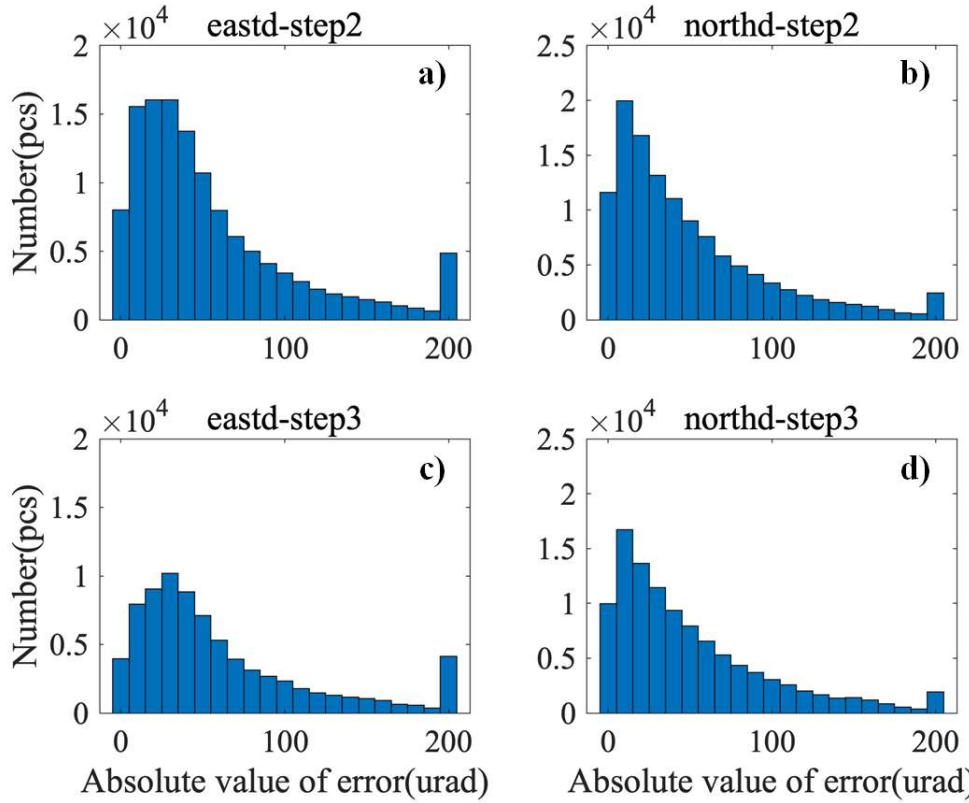
Figure 9. Noise histogram with different step sizes (a: east-west component at step size 2; b: north-south component at step size 2; c: east-west component at step size 3; d: north-south component at step size 3).

In addition, comparisons between step sizes were conducted in two other experimental areas, and the statistical results are presented in Table 3. It's interesting that experimental area 3 exhibits distinctive characteristics. Satellites with lower inclinations, such as the Topex/Poseidon and Jason series, are unable to provide observations beyond 66°, and area 3, a region with high ocean dynamics in the Southern Oceans, exhibits a noticeable decline in DOV quality in high-latitude regions.

Table 3. Statistics of DOV components with respect to V32.1 for different step sizes (unit: μrad)

Area	Step size	DOV components	Max	Min	Mean	STD
1	2	East-west	623.07	-610.62	-0.02	3.19
	3	East-west	258.74	-393.84	-0.02	2.37
	2	North-south	613.82	-614.79	0.01	2.02
	3	North-south	388.40	-401.70	0.01	1.75
2	2	East-west	326.62	-327.40	-0.03	2.40
	3	East-west	628.80	-286.61	-0.03	1.80
	2	North-south	327.37	-328.91	0.00	1.50
	3	North-south	400.27	-584.03	0.00	1.39
3	2	East-west	634.40	-639.41	0.11	5.41
	3	East-west	518.80	-644.39	0.09	4.34
	2	North-south	636.89	-634.96	-0.09	4.61
	3	North-south	620.09	-522.40	-0.10	3.74

4.3.2 Special processing in near-shore areas

Along the coastline, SSH measurements are typically available only on the ocean side, while grid points over land are default values and posing computational challenges. As illustrated in Figure 8, increasing the step size effectively reduced a considerable number of noise points over the open sea, while the remaining noise points majorly concentrated in near-shore areas. To demonstrate the effect of special processing in near-shore areas, we chose the China sea and its adjacent waters (100°-140°E, 0°-40°N) as the experimental area. This area is densely distributed with islands and reefs, involving typical categories of coastal regions. Based on the calculated residual DOV with respect to V32.1, we distinguished noise points where the absolute deviation exceeds 20 μrad. The distribution of noise points near the coastlines is more pronounced, as shown in Figure 10. The east-west component and north-south component noise points account for 0.27% and 0.09% of the total grid points in the region, respectively. It is evident that larger noise points are more prevalent in the anomalous computation of the east-west component. Therefore, special treatment is required in near-shore areas to mitigate the concentrated occurrence of noise. As previously mentioned, the Green's function method operates within a 64*64 grid area. When handling near-shore regions, the grids over land lack data, with controlling points only available on the ocean side. Thus, the actual data boundary is at the coastline, but not at the edges of the 64*64 grid. These mixed zones directly cause boundary effects that hinder matrix convergence. Expanding the computation area is not a feasible solution because even with an enlarged area, there are no effective data points over land to provide constraints. Solutions without constraints typically exhibit lower reliability, contributing significantly to the observed noise in coastal areas. Figure 11 further gives these differences between calculation and V32.1 over land-influenced 64*64 grid areas, showing the approximate outline of the block-wise rectangular computational regions in finer detail. The influential grid points in near-shore areas account for 10% of the total grid points. Additionally, there are 30% of grid points over land within the influential region, indicating a significant proportion of near-shore grid points.
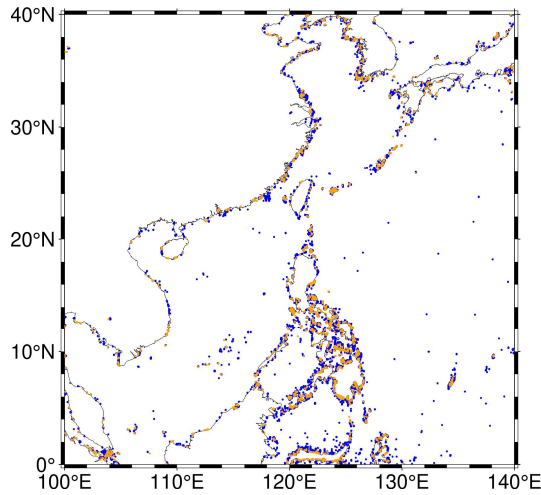
Figure 10. The main locations of noise distribution in the near-shore area
(east-west component in orange, north-south component in blue).
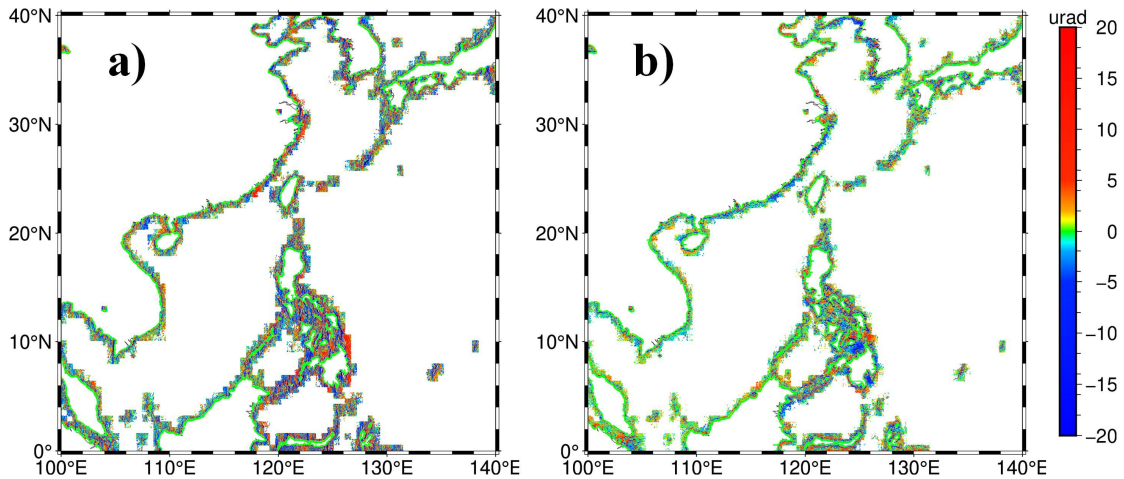
Figure 11. Location of distribution of nearshore areas disturbed by continental regions
(a: east-west component; b: north-south component).

To constrain this boundary effect, special processing steps were implemented. A continental mask was applied to identify controlling points over land, which were assigned a value of 0 and treated as known points. Moreover, these points were assigned relatively huge uncertainties to minimize their weight. This approach effectively mitigated boundary effects, thereby controlling data divergence and improving the reliability of computations in these land-influenced regions. Figure 12 illustrates the difference in nearshore points before and after processing. Following the adjustments, there is almost no change on the seaward side. Whereas on the landward side, the standard deviation shows a difference of 1.67 μrad in the east-west component and 1.47 μrad in the north-south component, with a maximum difference of around 60 μrad. This indicates that this special processing effectively suppressed the occurrence of large noise points near the coastlines.
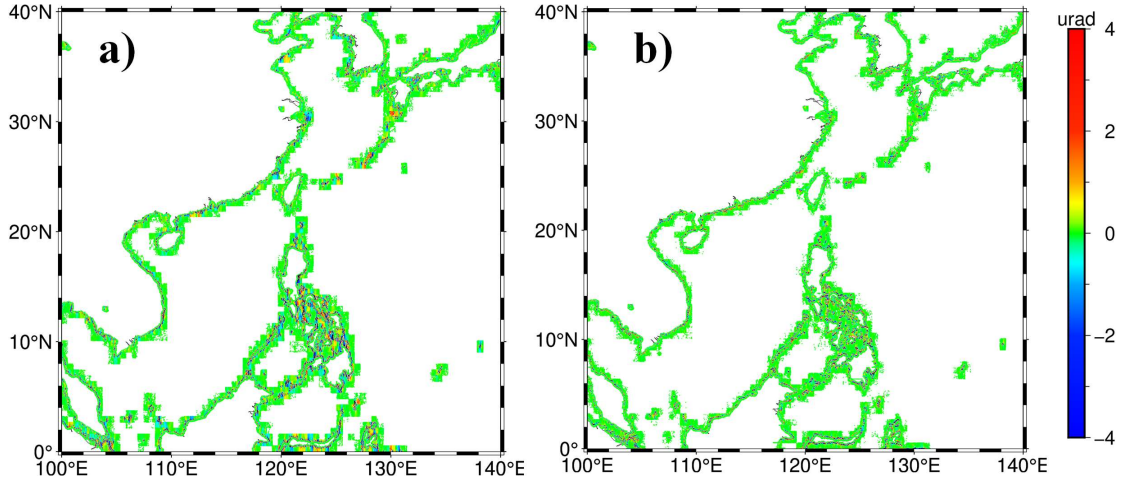
Figure 12. Difference in results in the nearshore area before and after the special processing (a: east-west component; b: north-south component).

Statistical analysis was also conducted in three experimental areas, and the results are listed in Table 4. The first and foremost is that the nearshore constraint effectively reduced the magnitude of maximum and minimum deviations. Especially in areas 1 and 2, maximum and minimum values were notably declined, indicating an effective constraint on the occurrence of large noise spikes. Moreover, similarly using a deviation threshold of 20 μrad for identifying noise points, the overall noise ratios decreased by 17.6% following this optimization effort.

Table 4. Statistics on the difference with respect to V32.1 with or without nearshore constraint (unit: μrad)

Area	Near-shore constraints	DOV components	Max	Min	Mean	STD
1	Yes	East-west	110.52	-96.43	-0.03	2.42
	No	East-west	258.74	-393.84	-0.02	2.37
	Yes	North-south	68.41	-87.66	0.02	1.76
	No	North-south	388.40	-401.70	0.01	1.75
2	Yes	East-west	95.22	-75.06	-0.03	1.77
	No	East-west	628.80	-286.61	-0.03	1.80
	Yes	North-south	81.95	-70.86	0.01	1.28
	No	North-south	400.27	-584.03	0.00	1.39
3	Yes	East-west	447.94	-644.39	0.09	4.35
	No	East-west	518.80	-644.39	0.09	4.34
	Yes	North-south	620.09	-461.79	-0.10	3.81
	No	North-south	620.09	-522.40	-0.10	3.74

4.3.3 Remove ERS-1 data

To evaluate the contribution of each individual mission to multi-satellite altimetry derived DOV, each satellite (SARAL/AltiKa, EnviSat, HY-2A/B, Geosat, and ERS-1) was sequentially removed within the China sea and its adjacent waters (100°-140°E, 0°-40°N). Median Absolute Deviations (MAD) of the east-west and north-south components along latitude were computed, with the

448   NSOAS24 DOV without data removal used as a comparison. Land-influenced zero values were

449   excluded during this experiment. The results were presented in Figure 13, which illustrates that

450   SARAL/AltiKa provides the most reliable data and the largest contribution. HY-2 also significantly

451   influences the DOV, resulting in discrepancies exceeding 2.5 µrad in the east-west component and

452   ranging from 1 to 1.5 µrad in the north-south component. ERS-1 and Geosat have a relatively minor

453   contribution, causing differences of less than 1.5 µrad and 1 µrad respectively in the east-west and

454   north-south components. This also suggests that their signals overlap to a greater extent with other

455   satellites.
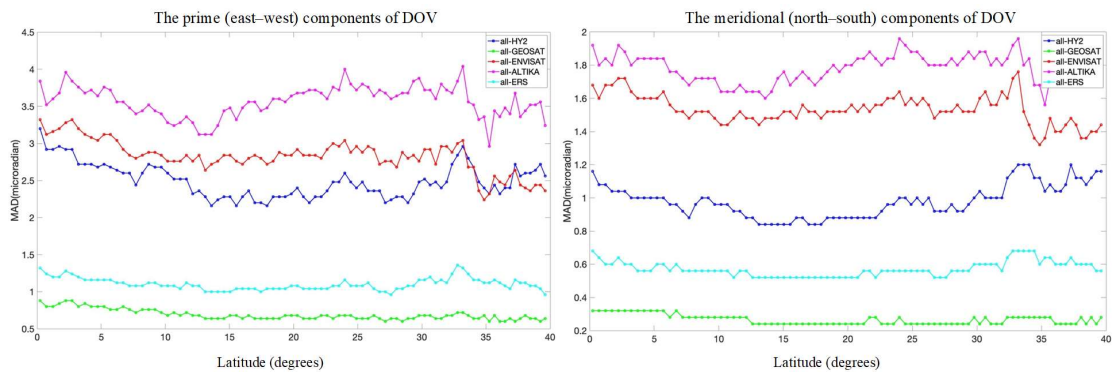
456

457   **Figure 13.** Difference in median absolute deviations between NSOAS24 DOV and DOV in the

458   absence of certain mission (The greater the difference, the larger the influence).

459   Additionally, DOV components were calculated for several single satellite mission, and the

460   MAD between them and V32.1 in latitude direction was compared. As shown in Figure 14, the

461   MAD values are consistently small for HY-2, ENVISAT, and SARAL/AltiKa. However, the data

462   from Geosat and ERS-1 exhibit significant deviations, suggesting considerably higher noise levels.
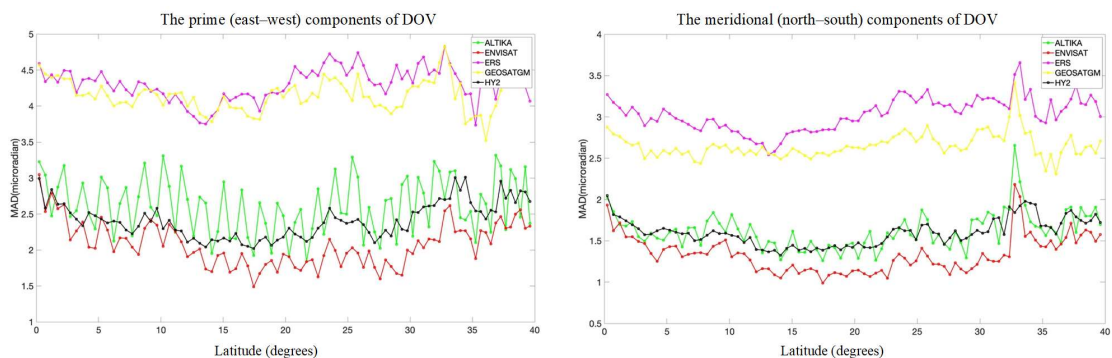
463

464   **Figure 14.** Difference in median absolute deviations between V32.1 DOV and the single satellite

465   solution (The smaller the difference, the better the DOV solution).

466   Due to being in the early stages of satellite altimetry, Geosat and ERS-1 may suffer from

467   inherent ranging errors and orbit determination issues that could lead to degraded data quality.

468   Considering the vast amount of observations accumulated in recent decades, it is worthwhile to

469   consider removing low-quality and redundant data. For Geosat, its extensive accumulated data

470   volume and dense coverage in high-latitude region, coupled with its unique 108° orbital inclination,

471   make it a distinct group of observations with independent direction. Therefore, we have chosen to

472   temporarily retain Geosat data in the NSOAS24 model construction. ERS-1 has also accumulated a

473   significant amount of data. However, within the same directional group in Table 2, SARAL/AltiKa

474   and Envisat share a substantial number of grid points that overlap completely with ERS-1

475   (accounting for 30.7% of overlap). During the gridding process, these overlapping data points were

476   stacked. In other words, 30.7% of ERS-1's data can be entirely replaced by higher-precision data

477   from SARAL/AltiKa and Envisat. From the perspective of controlling points, it is noteworthy that

478   control points in all directions exhibit a duplication rate exceeding 95%. Therefore, with adequate

479   data coverage, multidirectional and high-quality precise slope data are required. Considering the

480   previously identified poor performance and high replaceability, ERS-1 data has been ultimately

481   removed in NSOAS24 model construction.

482   **4.4 Gravity anomaly inversion procedure**

483   Based on the DOV components at grid points, the residual gravity anomalies were calculated

484   using the FFT method according to the Laplace Equation derived relationship, and the results were

485   shown in Figure 15. Finally, a global marine gravity model over a range of 80°S-80N° with a 1′×1′

486   grid interval, named NSOAS24, was constructed after restoring the removed reference model, as

487   shown in Figure 16.
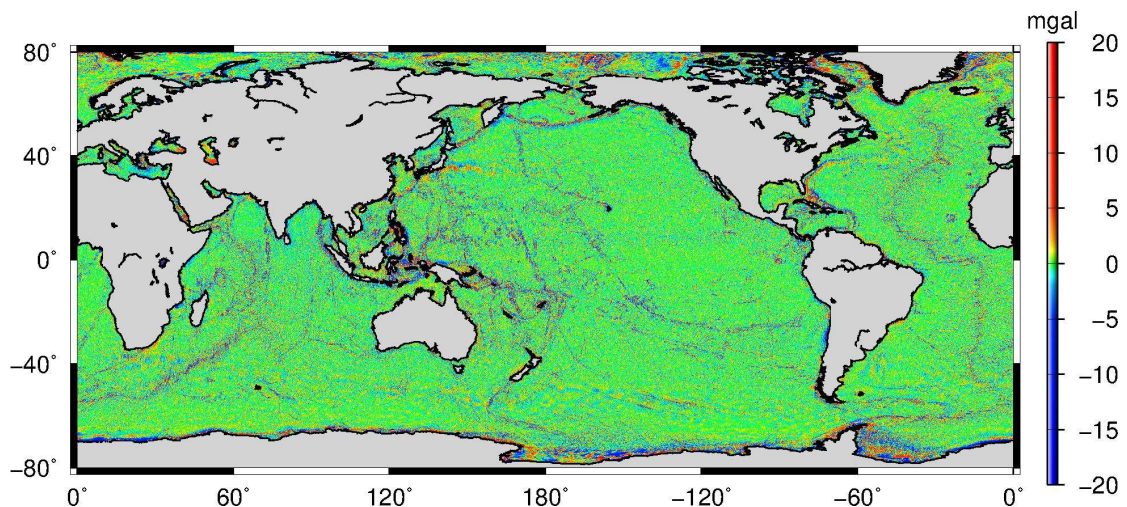
488
489   **Figure 15.** The residual gravity anomaly map of NSOAS24.
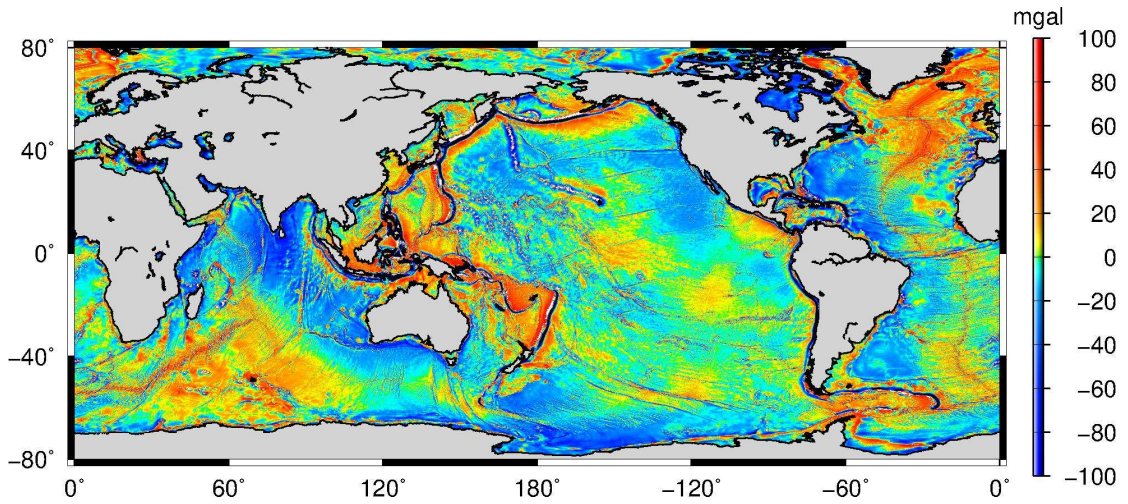
Figure 16. The gravity anomaly map of NSOAS24.

5 Gravity anomaly results

5.1 Comparison with V32.1 and DTU21

Firstly, the reliability of NSOAS24 was validated using altimetry-derived models, e.g., DTU21 and V32.1, with statistical results summarized in Table 5. In Area 1 with relatively complex seafloor terrains, which includes the Mariana Trench, seamount chains, and numerous nearshore areas, NSOAS24 shows improvements of 0.6 mGal and 1.2 mGal over its predecessor (NSOAS22), compared to DTU21 and V32.1, respectively. In the predominantly open sea Area 2, NSOAS24 demonstrates enhancements of 0.5 mGal and 0.7 mGal over NSOAS22, compared to DTU21 and V32.1, separately. Area 3 shows a 0.3 mGal improvement for NSOAS24 over NSOAS22, compared to DTU21, and a 1.0 mGal improvement compared to V32.1.

Table 5. Statistics of NSOAS24 and its predecessor against DTU21 and V32.1 (unit: mGal)

Area	Model	Max	Min	Mean	STD
1	NSOAS22-DTU21	202.64	-196.75	-0.09	3.56
	NSOAS24-DUT21	238.23	-255.97	0.02	2.93
	NSOAS22-V32.1	167.32	-196.69	-0.13	3.15
	NSOAS24-V32.1	91.36	-243.28	-0.03	1.97
2	NSOAS22-DTU21	71.89	-163.61	-0.07	1.96
	NSOAS24-DUT21	104.50	-72.45	-0.03	1.46
	NSOAS22-V32.1	63.64	-159.40	-0.05	1.95
	NSOAS24-V32.1	109.01	-101.60	-0.01	1.23
3	NSOAS22-DTU21	90.40	-167.89	0.02	6.32
	NSOAS24-DUT21	195.52	-223.07	0.02	6.01

NSOAS22-V32.1	329.41	-195.06	-0.08	4.63
NSOAS24-V32.1	305.43	-188.36	-0.08	3.61

5.2 Comparison with shipborne gravity data

The distribution of shipborne data and corresponding gravity anomalies of NSOAS24 model in three experimental areas are illustrated in Figure 17. In Area 1, NCEI data show relatively even distribution, while JAMSTEC data are concentrated near Japan with dense nearshore coverage. In Area 2, NCEI data are involved within entire region, while FOCD and SHOM data are primarily concentrated along the Mid-Atlantic Ridge. In Area 3, NCEI data are sparse, with fewer observations, whereas MGDS data are more evenly distributed and voluminous. Statistical comparisons are presented in Table 6. The analysis highlights that NSOAS24 significantly improves accuracy compared to NSOAS22. Furthermore, NSOAS24 demonstrates accuracy comparable to DTU21 and V32.1, and outperforms V32.1 in the high-latitude polar regions.

Finally, these models were validated using worldwide distributed shipborne data. The accuracy of each model was assessed using two sets of shipborne data: the early NCEI dataset and the recent high-quality dataset from JAMSTEC, MGDS, FOCD, and SHOM. The results are summarized in Table 7. In general, NSOAS24 demonstrates accuracy comparable to DTU21 and V32.1. Compared to its predecessor, NSOAS24 shows a steady improvement in accuracy, with a reduction of ~0.7 mGal in standard deviations when compared with recent non-NCEI shipborne data.
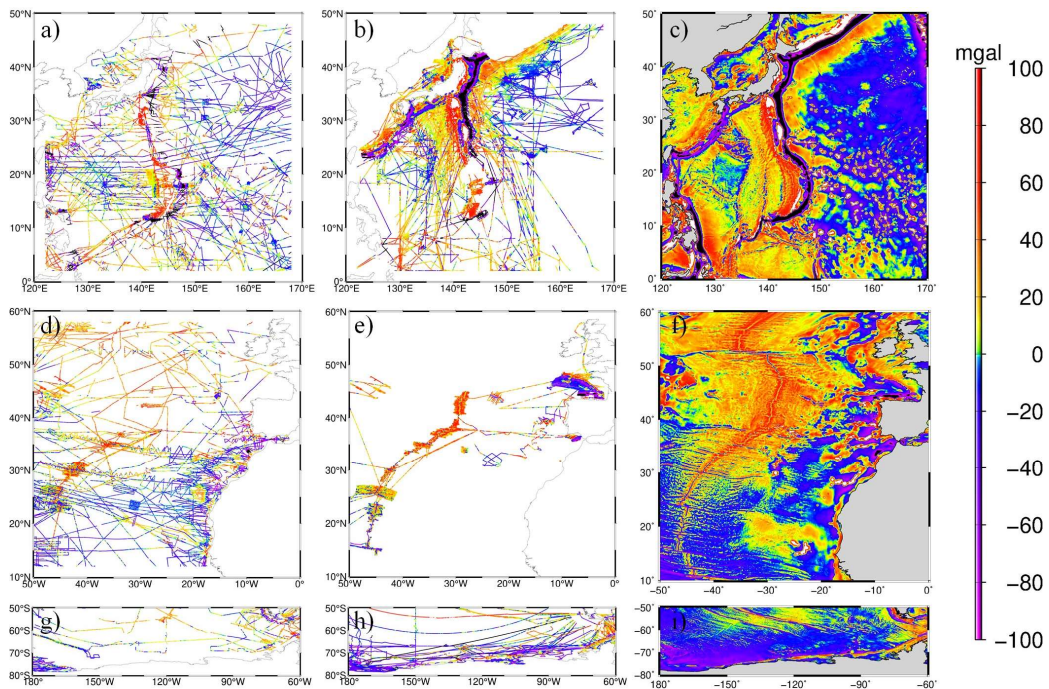
Figure 17. Distribution of NCEI and non-NCEI shipborne data, and recovered gravity anomalies.

Table 6. Statistics on differences between altimeter-derived models and shipborne gravity data (unit: mGal)

Area	Model	Ship-borne data	Max	Min	Mean	STD	Ship-borne data	Max	Min	Mean	STD
1	NSOAS22	NCEI	55.82	-45.38	-0.52	6.14	JAMSTEC	40.20	-42.62	0.97	5.18
	NSOAS24		37.07	-41.06	-0.68	5.60		35.15	-42.88	1.12	4.97
	DTU21		36.09	-42.72	-0.72	5.12		24.90	-26.20	0.56	4.37
	V32.1		54.68	-68.25	-0.68	5.07		57.91	-66.35	0.74	4.99
	EGM2008		15.00	-15.00	-0.61	5.70		15.00	-15.00	0.52	4.93
2	NSOAS22	NCEI	33.02	-29.06	3.07	7.28	FOCD SHOM	29.74	-31.69	2.93	6.95
	NSOAS24		27.35	-27.61	3.24	7.21		26.67	-25.17	3.17	6.60
	DTU21		23.96	-22.73	3.16	7.17		22.14	-18.70	3.14	6.48
	V32.1		36.84	-26.69	3.19	7.19		29.45	-19.20	3.16	6.45
	EGM2008		15.00	15.00	2.87	7.13		15.00	15.00	2.78	6.74
3	NSOAS22	NCEI	35.16	-46.12	2.54	6.40	MGDS	39.72	-43.68	-0.10	6.18
	NSOAS24		189.58	-38.36	2.56	6.21		44.94	-68.45	-0.09	5.92
	DTU21		23.28	-41.36	3.20	5.79		44.68	-58.59	0.16	5.83
	V32.1		279.57	-142.13	2.64	7.79		235.69	-114.62	0.41	8.68
	EGM2008		15.00	15.00	2.42	6.28		15.00	15.00	-0.08	6.19

Table 7. Verifications with globally distributed shipborne data (unit: mGal)

Model	Ship-borne data and number(pcs)	Max	Min	Mean	STD	Ship-borne data and number(pcs)	Max	Min	Mean	STD
NSOAS22	NCEI (10740231)	56.39	-67.77	1.48	6.64	JAMSTEC	48.46	-48.02	1.00	5.64
NSOAS24		183.63	-134.00	1.49	6.33	MGDS	48.08	-156.23	1.01	4.95
DTU21		46.37	-57.59	1.34	6.20	FOCD	44.68	-81.73	0.71	4.71
V32.1		279.59	-193.98	1.41	6.40	SHOM	297.00	-114.62	0.86	5.53
EGM2008		15.00	-15.00	1.24	6.33	(33522351)	15.00	-15.00	0.67	5.20

6 Conclusions

Based on our global marine gravity model construction experience in NSOAS22, we initially optimized the dataset by incorporating recent observations and excluding highly substitutable ERS-1 data. Then, multi-satellite datasets were uniformly prepared for constructing a new global marine gravity model. During the processing, satellites with different orbital inclinations were firstly grouped into 5 categories. For multi-cycle ERM data, they were appended to the same data file in a way that preserves the temporal continuity of the data without disruption. Secondly, raw waveforms were retracked using the two-step weighted least-square retracker, and high-rate observations along profiles were uniformly resampled into 5 Hz to enhance the density of available measurements. Thirdly, pre-processing and slope editing were applied to the SSH measurement data to remove outliers, and the Parks–McClellan filter was used to constrain the amplified high-frequency noise during the differencing procedure. Fourthly, the residual along-track DOV was calculated from slopes by dividing by corresponding along-track velocities and introducing EGM2008 as a reference model. Fifthly, gridded DOV were determined from along-track DOV by the Green's function

method. Finally, a global marine gravity model was constructed after FFT and corresponding inverse transform, restoring the removed reference model.

Comparing with the predecessor NSOAS22, several optimizations and improvements were implemented during the entire processing procedures for building NSOAS24. (1) Employing block-based input and output, calculations were executed with a 64*64 grid input and output the central 32*32 grid. This improvement effectively resolved poor accuracy issues at boundaries and eliminated discontinuities between adjacent regions. (2) Utilizing the Green's function method to solve the DOV components, we increased the step size from 2 to 3 for selecting grid points as control points for iteration. This optimization aimed to enhance computational efficiency, reduce matrix complexity, and achieve noise smoothing effects. (3) We implemented specialized processing in coastal regions by incorporating a continental mask. The identified land points were assigned a default value with huge uncertainty to mitigate their weight. This approach effectively suppressed boundary effects near coastlines and controlled data divergence.

The new NSOAS24 model was firstly validated with well-known altimetry derived models. Comparisons were made in three experimental areas (Low-latitude, Mariana Trench area; mid-latitude: Mid-Atlantic Ridge area. High-latitude, Antarctic area) against the DTU21 and V32.1. Compared to the predecessor NSOAS22, NSOAS24 showed improvements of 0.6 mGal, 0.5 mGal, 0.3 mGal, and 1.2 mGal, 0.7 mGal, 1.0 mGal, respectively. Next, we utilized two sets of shipborne data to verify the new model: the earlier NCEI dataset and the recent non-NCEI dataset collected from JAMSTEC, MGDS, FOCD, SHOM. NSOAS24 also demonstrated a steady improvement in accuracy compared to NSOAS22. Finally, on a global scale, we validated NSOAS24 (6.33 mGal and 4.95 mGal) using the NCEI dataset and the combined dataset from JAMSTEC, MGDS, FOCD, and SHOM (6.20 mGal and 4.71 mGal for DTU21; 6.40 mGal and 5.53 mGal for V32.1). NSOAS24's accuracy was comparable to DTU21 and V32.1, with a notable improvement over NSOAS22 (6.64 mGal and 5.64 mGal). It is worth mentioning that NSOAS24 showed a decline in standard deviations of around 0.7 mGal compared to NSOAS22 when comparing with non-NCEI data. In conclusion, validations with both altimetry-derived models and shipborne data proved the effectiveness of optimizations and reliability of the NSOAS24 model.

Author contributions

SZ and RZ contributed to the development of the global marine gravity anomaly model. Writing of the original draft was undertaken by XC and SZ, and YJ contributed to review and editing. All authors checked and gave related comments for this work.

Data availability

The global marine gravity anomaly model, NSOAS24, is available at the ZENODO repository, https://doi.org/10.5281/zenodo.12730119 (Zhang et al., 2024). The dataset includes global marine gravity anomalies in NetCDF file fortmat.

Competing interests

The contact author has declared that none of the authors has any competing interests.

Acknowledgements

We are very grateful to AVISO for providing the altimeter data, and NCEI, JAMSTEC, MGDS, FOCD, SHOM for providing shipborne gravity. We are also thankful to SIO and DTU for their published altimetry derived gravity models. Thanks to ICGEM for providing earth gravity models.

Financial support

This study was supported by the National Nature Science Foundation of China, grant number 421932513.

References

Andersen O. B., Knudsen P.: The DTU17 global marine gravity field: First validation results. In: International Association of Geodesy Symposia, Springer: Berlin/Heidelberg, Germany, https://doi.org/10.1007/1345_2019_65, 2019.

Andersen, O. B., Rose, S. K., Abulaitijiang, A., Zhang, S., & Fleury, S.: The DTU21 global mean sea surface and first evaluation, Earth System Science Data Discussions., 1-19. https://doi.org/10.5194/essd-15-4065-2023, 2023.

Brammer, R. F., Sailor, R. V.: Preliminary estimates of the resolution capability of the Seasat radar altimeter, Geophysical Research Letters., 7(3), 193-196,

592   https://doi.org/10.1029/GL007i003p00193, 1980.

593   Chen, X., Kong, X., Zhou, R., Zhang, S.: Fusion of altimetry-derived model and ship-borne data in
594   preparation of high-resolution marine gravity determination, Geophysical Journal
595   International., 236(3):1262–1274, https://doi.org/10.1093/gji/ggad471, 2024.

596   Fu, L.-L. and Cazenave, A.: Satellite altimetry and earth sciences: ahandbook of techniques and
597   applications, Academic, San Diego, United States, ISBN 978-0-12-269545-2, 493 pp., 2001.

598   Guo, J., Luo, H., Zhu, C., Ji, H., Li, G., Liu, X.: Accuracy comparison of marine gravity derived
599   from HY-2A/GM and CryoSat-2 altimetry data: a case study in the Gulf of Mexico,
600   Geophysical Journal International., 230(2):1267–1279, https://doi.org/10.1093/gji/ggac114,
601   2022b.

602   Hao, R., Wan, X., Annan, R.F.: Enhanced Short-Wavelength Marine Gravity Anomaly Using Depth
603   Data, IEEE Transactions on Geoscience and Remote Sensing., 61, 1-9,
604   https://doi.org/10.1109/TGRS.2023.4242967, 2023.

605   Li, Q., Bao, L., Wang, Y.: Accuracy Evaluation of Altimeter-Derived Gravity Field Models in
606   Offshore and Coastal Regions of China. Front. Earth Sci., 9, 722019,
607   https://doi.org/10.3389/feart.2021.722019, 2021.

608   Mohamed, A., Ghany, R.A.E., Rabah, M., Zaki, A.: Comparison of recently released satellite
609   altimetric gravity models with shipborne gravity over the Red Sea. Egypt. J. Remote Sens.
610   Space Sci., 25, 579–592, https://doi.org/10.1016/j.ejrs.2022.03.016, 2022.

611   Pavlis, N.K., Holmes, S.A., Kenyon, S.C., Factor, J.K.: The development and evaluation of the Earth
612   Gravitational Model 2008 (EGM2008), J. Geophys. Res., V117, B04406,
613   https://doi.org/10.1029/2011JB008916, 2012.

614   Sandwell, D.T., Harper, H., Tozer, B., Smith, W.H.F.: Gravity field recovery from geodetic altimeter
615   missions. Adv. Space Res., 68, 1059–1072, https://doi.org/10.1016/j.asr.2019.09.011, 2021.

616   Sandwell, D.T., Smith, W.H.: Marine gravity anomaly from Geosat and ERS 1 satellite altimetry.,
617   Journal of Geophysical Research:Solid Earth., 102(B5): 10039-10054,
618   https://doi.org/10.1029/96JB03223, 1997.

619   Stammer, D. and Cazenave, A.: Satellite altimetry over oceans and land surfaces, CRC Press, Boca
620   Raton, https://doi.org/10.1201/9781315151779, 2017.

621 Wan, X., Annan, R.F., Jin, S., Gong, X.: Vertical deflections and gravity disturbances derived from
622   HY-2A Data, Remote Sens., 12(14), 2287, https://doi.org/10.3390/rs12142287, 2020.

623 Wan, X., Hao, R., Jia, Y., Wu, X., Wang, Y., Feng, L.: Global marine gravity anomalies from multi-
624   satellite altimeter data, Earth Planets Space., 74, 165, https://doi.org/10.1186/s40623-022-
625   01720-4, 2022.

626 Wessel, P., Bercovici, D.: Interpolation with Splines in Tension: A Green's Function Approach,
627   Mathematical Geology., 30, 77–93, https://doi.org/10.1023/A:1021713421882, 1988.

628 Zhang, S., Andersen, O.B., Kong, X., Li, H.: Inversion and validation of improved marine gravity
629   field recovery in South China Sea by incorporating HY-2A altimeter waveform data, Remote
630   Sensing., 12(5):802, https://doi.org/10.3390/rs12050802, 2020.

631 Zhang, S., Chen, X., Zhou, R., Jia, Y.: A new global marine gravity model NSOAS24 derived
632   from multi-satellite sea surface slopes, Zenodo [Data set],
633   https://doi.org/10.5281/zenodo.12730119, 2024.

634 Zhang, S., Sandwell, D.T.: Retracking of SARAL/AltiKa radar altimetry waveforms for optimal
635   gravity field recovery, Marine Geodesy., 40(1), 40–56,
636   https://doi.org/10.1080/01490419.2016.1265032, 2017.

637 Zhang, S., Zhou, R., Jia, Y., Jin, T., Kong, X.: Performance of HaiYang-2 Altimetric Data in Marine
638   Gravity Research and a New Global Marine Gravity Model NSOAS22, Remote Sens., 14, 4322,
639   https://doi.org/10.3390/rs14174322, 2022.

640 Zhu, C., Guo, J., Gao, J., Liu, X., Hwang, C., Yu, S., Yuan, J., Ji, B., and Guan, B.: Marine gravity
641   determined from multi-satellite GM/ERM altimeter data over the South China Sea: SCSGA
642   V1.0, J. Geodesy, 94, 50, https://doi.org/10.1007/s00190-020-01378-4, 2020.

643 Zhu, C., Guo, J., Yuan, J., Li, Z., Liu, X., & Gao, J.: SDUST2021GRA: Global marine gravity
644   anomaly model recovered from Ka-band and Ku-band satellite altimeter data, Earth System
645   Science Data., 1-23, https://doi.org/10.5194/essd-14-4589-2022, 2022.